

Copyright © 1984, by the author(s).
All rights reserved.

Permission to make digital or hard copies of all or part of this work for personal or classroom use is granted without fee provided that copies are not made or distributed for profit or commercial advantage and that copies bear this notice and the full citation on the first page. To copy otherwise, to republish, to post on servers or to redistribute to lists, requires prior specific permission.

ELECTRON BEAM TIME-OF-FLIGHT MEASUREMENTS
OF PLASMA POTENTIAL IN TANDEM MIRRORS

by

M. A. Lieberman and C. P. Chang

Memorandum No. UCB/ERL M84/92

8 November 1984

cover

ELECTRON BEAM TIME-OF-FLIGHT MEASUREMENTS
OF PLASMA POTENTIAL IN TANDEM MIRRORS

by

M. A. Lieberman and C. P. Chang

Memorandum No. UCB/ERL M84/92

8 November 1984

ELECTRONICS RESEARCH LABORATORY

College of Engineering
University of California, Berkeley
94720

6th page

Research sponsored by Department of Energy Contract DE-AT0E-76ET53059.

TABLE OF CONTENTS

A.	Introduction	3
B.	Potential Barrier Measurements in the MMX	5
C.	Remote Detection Using Neutral Atom Targets	12
D.	Remote Detection Using Plasma Ion Targets	22
E.	Remote Detection Using Beam Magnetic Fields	27
F.	Electron Beam-Plasma Instabilities	32

A. Introduction

In this report we describe an electron beam time-of-flight measurement of the thermal barrier potential in the Berkeley Multiple Mirror Experiment (MMX), and we examine the feasibility of using the technique to measure the space and time resolved plasma potential in large tandem mirror experiments.

The measurement is performed by propagating a series of electron beam pulses along a magnetic field line from one end of a mirror device to the other (see Fig. 1). The beam electrons slow down or speed up as they move into regions of negative or positive plasma potential, respectively. By observing the time-of-flight of the beam pulses between two nearby detecting stations, the beam velocity, and thus the corresponding plasma potential, can be determined.

For the actual measurements on the MMX that we report here (see Sec. B), a negative thermal barrier potential is created in one mirror cell of the MMX by short pulse, electron cyclotron resonance heating (ECRH). This barrier is subsequently destroyed on the timescale for passing ions to become trapped in the heated cell. The timescale is 30-50 μsec for $T_i = T_e \approx 12$ eV, $T_h \approx 1$ keV, $n \approx 5 \times 10^{11} \text{cm}^{-3}$ typical in the MMX. The time-of-flight measurement we have developed has been used to make detailed measurements of barrier potential for a single MMX discharge on timescales as short as 5 μsec with a potential resolution as small as ± 5 volts. The measurements are corroborated by a number of additional diagnostics.

In the MMX, the time-of-flight is measured by means of a collector probe physically inserted into the plasma so as to intercept the beam current. The time-of-flight can be measured on larger (hotter) tandem mirror devices only if the beam can be remotely sensed. We have examined three remote sensing techniques which are illustrated in Fig. 1: (a) beam collisions with plasma neutrals, yielding optical line radiation (described in Sec. C); (b) beam collisions

with plasma ions, yielding x-ray bremsstrahlung (described in Sec. D); and (c) beam current-induced magnetic fields (described in Sec. E).

For all techniques, sources of noise exist, and signal averaging methods must be used to increase the signal-to-noise ratio. For a given time resolution, the extraction of the signal from the noise sets a limit on the use of the time-of-flight measurement.

In Sec. C, we examine the noise sources and the required signal averaging methods. We estimate the rms uncertainty on the measured potential due to the noise, and give the scaling of this uncertainty with the plasma and beam parameters. We give numerical estimates of plasma and beam parameters to illustrate the feasibility of each remote sensing technique. In Sec. F, we also examine the effects of beam-plasma instabilities and consider their importance to the measurement techniques.

Our results are as follows: (a) Optical line radiation techniques appear feasible in TMX-U, especially in the low density mode of operation. A major uncertainty is the neutral D density within the hot core at the measurement stations. (b) X-ray bremsstrahlung techniques may only be feasible in TMX-U at the very highest densities, but may be more attractive in MFTF-B. A major uncertainty is the level of bremsstrahlung produced by ECRH hot electrons at the measurement stations. (c) Beam current, magnetic field techniques appear feasible for both low and high density tandem mirrors. However, major uncertainties are the spectral power density for plasma-produced magnetic field noise near the beam modulation frequency, and possible current neutralization of the beam.

For all three techniques, the limitations due to beam-plasma instabilities are probably not too serious. The critical issues that must be addressed in future studies are (1) noise levels and (2) received signal strengths.

B. Potential Barrier Measurements in the MMX

A negative electrostatic potential barrier has been created in one mirror cell of the MMX by means of ECRH. The potential during the formation and destruction of the barrier has been measured using the electron beam time-of-flight diagnostic, with a resolution of ± 5 volts on a 5 microsecond timescale.

The measurements are performed in the magnetic mirror system (MMX) shown in Fig. 2. The magnetic field is pulsed, with a rise time of 200 μ sec and a decay time of 2 μ sec. Plasma injected from a Marshall gun source flows along a 225 cm, 0.18 T, axial magnetic field and through a mirror-quadrupole field at T_8 into three cells with midplanes at M_{56} , M_{67} , and M_{78} . Each cell has length $l = 75$ cm and midplane field $B_0 = 0.18$ T. The last cell at M_{56} is terminated in a mirror-quadrupole field at T_6 and T_7 having mirror ratio $R = 2.8$ and fan ellipticity $Q \approx 20$.

The 10 cm diameter metal chamber wall of the central cell, together with mesh-covered endplates at T_6 and T_7 having openings shaped to fit the elliptical flux surfaces, form a cavity for ECRH that does not obstruct the plasma flow. A 3 μ sec, 250 kW, 9.0 GHz, rf heating pulse is injected into the plasma-filled cavity at M_{67} . This creates a magnetically confined, hot electron density n_h in the center cell due to ECRH at the two resonance zones, each 6 cm from the mirror throats.

The sudden appearance of the hot-electron population, and the corresponding reduction of the cold-electron population, initiates formation of a negative potential barrier near throats T_6 and T_7 as follows: The potential V_7 of midplane M_{67} with respect to midplane M_{78} is related to the cold (non-magnetically confined) electron densities n_{67} and n_{78} by the Boltzmann relation. If $n_{67} < n_{78}$, a negative potential barrier forms near T_7

$$V_7 = -T_c \ln(n_{78}/n_{67}) , \quad (1)$$

where T_c is the cold-electron temperature. A similar expression determines V_6 . These expressions are invalid in the limit $n_{67} \rightarrow 0$, where the ion flow dynamics must be considered. For this case, the potentials can be estimated by equating the total ion flux to the total electron flux entering the center cell. Using, for example, a Bohm velocity for the ions, we have (for $V_6, V_7 < 0$)

$$(n_{58} + n_{78})(T_c / \varepsilon m_i)^{1/2} = [n_{58} \exp(V_6 / T_c) + n_{78} \exp(V_7 / T_c)](8T_c / \pi m)^{1/2} \quad (2)$$

where m_i and m are the ion and electron masses and ε is the natural base. Assuming, for simplicity, that the Boltzmann relation is valid for the densities and potentials between M_{58} and M_{78} ,

$$n_{58} \exp(V_6 / T_c) = n_{78} \exp(V_7 / T_c) , \quad (3)$$

we obtain

$$V_7 = T_c \left[\ln\left(1 + \frac{n_{58}}{n_{78}}\right) - \frac{1}{2} - \frac{1}{2} \ln\left(\frac{2m_i}{\pi m}\right) \right] . \quad (4)$$

A similar expression holds for V_6 . For hydrogen ions with $n_{58} = n_{78}$, we find

$$V_7 = V_6 \approx -3.3 T_c . \quad (5)$$

The potential barrier is destroyed on the timescale for ions to enter into and become trapped in the center cell. By quasi-neutrality, cold electrons accompany the trapped ions, and therefore n_{67} increases on the ion trapping timescale. The final state in this idealized model ($n_{58} = n_h = n_{78} = \text{const}$ and $T_c = \text{const}$, initially) is $n_{67} = n_h$ and $V_6 = V_7 = 0$. The total electron density (hot + cold) rises to twice its initial value after barrier destruction. Non-ideal effects important in the experiment include: initial axial density variations,

non-zero ion transit time, heating of cold electrons by hot electrons, and plasma loss processes during barrier formation and decay.

The electron beam probe system, illustrated in Fig. 3, consists of an electron gun located at M_{78} and a beam collector at M_{58} . The electron gun generates an electron beam having current $I_b \approx 100 \mu\text{A}$ and voltage $V_b = 150\text{--}200$ V that propagates along the magnetic axis to the collector. The gun consists of a tungsten filament and grid located inside a 0.32 cm diameter, stainless steel tube. A 0.32 cm diameter, mesh-covered hole in the side of the tube serves as the gun anode. The beam collector is identical in construction, with the filament replaced by a collector plate.

To determine beam time-of-flight, the beam current is modulated at $f = 10$ MHz, and the phase delay of the signal received at the collector is measured. To provide high signal-to-noise ratio, a digital, phase-locked loop is used. The beam modulation is synchronized to a 100 MHz transient digitizer, and the received current, after passing through a tuned amplifier ($v_{out} = 4 \times 10^4 i_{in}$, $f = 10$ MHz, $\Delta f \approx 1.3$ MHz), is digitized. The 32 k samples are processed subsequently as follows: A sine wave is fitted to each group of twenty consecutive samples, and its amplitude A_j and phase φ_j are determined by a least square error criterion. Fifty consecutive values of $\sin \varphi_j$ (and $\cos \varphi_j$) so determined are then averaged to obtain the mean phase φ and its standard deviation s over the five or ten microsecond sampling interval. It is easily seen that the standard deviation for a set of phases φ_j chosen randomly from the interval $(0, 2\pi)$ is $\pi/3$. Thus measured phases having $s > 0.6$ are not considered significant.

The phase $\varphi(x)$ due to an axial potential distribution $V(x)$, with respect to the beam cathode at $x = 0$, is given by

$$\varphi(x) = \omega t(x) = \omega \int_0^x \frac{dx}{v(x)} \quad (6)$$

where

$$v(x) = \left(\frac{2eV(x)}{m} \right)^{1/2}$$

is the beam velocity. If we assume a simple square well model for the potential (see Fig. 4), then the phase change $\Delta\varphi$ at $x = 2l$ due to the creation of a negative barrier of magnitude Φ_{bar} and length l is

$$\Delta\varphi = \frac{\omega l}{v_b} \left[\left(1 - \frac{\Phi_{\text{bar}}}{V_b} \right)^{-1/2} - 1 \right]. \quad (7)$$

For $\Phi_{\text{bar}} \ll V_b$, we find

$$\Delta\varphi \approx \frac{1}{2} \frac{\omega l}{v_b} \frac{\Phi_{\text{bar}}}{V_b}. \quad (8)$$

Equation (8) has been verified experimentally by applying a -45 V, 100 μsec pulse to a 2.5 cm diameter ring electrode placed on axis at the midplane of the center cell. The dependence of $\Delta\varphi$ on V_b in (7) has also been verified over the range from 100 to 200 volts. Finally, the time response of the beam diagnostic has been measured by applying a 20 V, peak-to-peak, 25 kHz square wave modulation in series with the cathode voltage. These measurements yield a response time that is less than 5 μsec .

Figure 5a shows the raw data $v_{\text{out}}(t)$ versus t for a single plasma discharge shot, with the ECRH applied at $t = 0$. Although ten samples of v_{out} per modulation period $1/f$ are digitized, only every other sample is plotted in the figure. If the output were a constant amplitude sinusoid at the frequency f , then five horizontal lines of "dots" should appear. The successive dots on each line are separated by exactly one modulation period. This behavior can be seen in the time interval before ECRH. Variations in signal amplitude and phase cause the lines to vary with time; noise produces a scattering in the dots for each line. This behavior can be seen in the figure, especially after ECRH. Figure 5b shows

the behavior of the phase delay $\Delta\varphi$ versus time after the data reduction to increase the signal-to-noise ratio. The phase is constant before ECRH, and abruptly increases by about 1.2 radians after heating. Using (7), this increase corresponds to a barrier $\Phi_{\text{bar}} \approx 65$ V. The standard deviations s of the reduced data are small except during the first 10-20 μsec after ECRH, when the noise from the pulsed magnetron power supply and/or the sudden plasma heating dominates. After the initial phase delay, the phase change returns toward its initial value on a 50 μsec time scale.

In addition to the electron beam diagnostic, the following diagnostics are also used: A swept frequency 35 GHz microwave interferometer in the central cell midplane M_{67} measures the total electron density n_{67} at 6 μsec intervals. A silicon, lithium-drifted, x-ray detector at M_{67} measures the hot-electron temperature T_h and the hot-electron decay rate. A diamagnetic loop at M_{67} determines the hot-electron $n_h T_h$ product. A nude, fast ionization gauge is used to determine the increase in gas pressure due to the firing of the plasma source and the emission of neutrals from the chamber walls. Sets of Langmuir probes at M_{58} and M_{78} are used to determine the electron densities n_{58} and n_{78} and floating potentials in these cells. Voltage-swept Langmuir probes are used to determine the electron temperatures T_{58} and T_{78} . Emitting probes are used to measure the plasma potentials V_{58} and V_{78} . Probes cannot be used in the central cell M_{67} during ECRH, due to arcing at the probe tips, and destruction of the hot electron distribution.

Figure 6 shows the set of data for the single plasma discharge shot of Fig. 5, having strong ECRH. In Fig. 6a, the x-ray pulses observed after ECRH are intense and persist over the entire 200 μsec interval. In Fig. 6b, the ion saturation current of a Langmuir probe in M_{78} , adjacent to the ECRH cell M_{67} , shows an initial increase in density (and possibly temperature), followed by a decay

over 20 μsec back to its initial value. A similar behavior is seen in Fig. 6c for the density in M_{67} , as measured with the swept interferometer. Finally, Fig. 6d shows the phase delay measured by the electron beam diagnostic. The maximum phase change $\Delta\varphi \approx -1.2$ radians corresponds to a negative barrier, from (7), of $\Phi_{\text{bar}} \approx 65$ volts.

To understand the time dependent behavior of the measured density and phase change in the ECRH cell, a one-dimensional, three cell model of the ion and electron flows into and out of the cell has been developed. The model incorporates the following assumptions and effects:

- (a) The cold electron and the ion temperature is $T_c = \text{const}$.
- (b) A square well potential barrier is used.
- (c) Charge neutrality is valid for all times.
- (d) Finite ion transit times are included.
- (e) Partial ion trapping due to collisional scattering is included.
- (f) Production of cold plasma by hot-electron ionization of neutrals is described.

For $T < 0$ (before ECRH), the potentials across the two cells are determined from the cold electron densities through the Boltzmann relations. These densities are known from Langmuir probe and microwave interferometer measurements. For $t > 0$ (after ECRH), the equations for the two potentials are found by requiring that net charge must not flow across either of the two cell interfaces (see Fig. 7):

$$\Gamma_{e1} - \Gamma_{i1} = \Gamma_{e2} - \Gamma_{i2} - (1 - X_i^*) \Gamma_{i3}^* \quad (9)$$

$$\Gamma_{e3} - \Gamma_{i3} = \Gamma_{e2} - \Gamma_{i2} - (1 - X_i^*) \Gamma_{i1}^* \quad (10)$$

Here the Γ 's are the particle fluxes, X_i is the ion trapping fraction, and "*"

denotes evaluation at a time that is delayed by an ion transit time τ_i ; e.g.,

$$\Gamma_{i3}^*(t) = \begin{cases} 0 & , t < \tau_i \\ \Gamma_{i3}(t-\tau_i) & , t > \tau_i \end{cases}$$

etc. We also require the rate equation for ion (and, by quasi-neutrality, cold electron) trapping in the heated cell:

$$\frac{dn_{i2}}{dt} = \frac{1}{l} \left[\Gamma_{i1} + \Gamma_{i3} - 2\Gamma_{i2} - (1-X_i)(\Gamma_{i1}^* + \Gamma_{i3}^*) \right] + S_{hn} \quad (11)$$

where

$$S_{hn} = \nu_{hn} n_h(t)$$

is the cold plasma production rate due to hot electron ionization of neutrals.

Equations (9)-(11) have been solved numerically using a finite difference method for given values of $n_{i1}(t)$ and $n_{i3}(t)$, known from Langmuir probe measurements, the given initial value $n_{i2}(0) = n_0$, known from the interferometer measurement, the temperature T_c , known from swept probe measurements, the neutral pressure, known from fast ion gauge measurements, the potential V_3 of cell 3 with respect to the chamber wall, known from emissive probe measurements, and a choice of initial cold electron density $n_{c2}(0)$. A numerical solution for the data of Fig. 6 with $n_{c2}(0) = 0.01 n_{i2}(0)$ is shown in Fig. 8. The barrier potential in Fig. 8a has a maximum amplitude of $3.5 T_c$ and decays on a timescale of about $40 \mu\text{sec}$. The cold electron density in Fig. 8b rises abruptly to $\sim n_0/2$. The total electron density (hot + cold) in Fig. 8c and the phase shift in Fig. 8d are roughly similar to the actual density and phase shift seen in Fig. 6c and Fig. 6d, respectively. The essential features of the experimental observations seem to be modeled quite well in the theory. However, the timescale for the theoretical phase shift is somewhat shorter than that seen experimentally. Further studies will be necessary to bring the theory and experiment into closer

agreement.

C. Remote Detection Using Neutral Atom Targets

1. Measurement technique

In this section we present quantitatively the measurement technique and obtain expressions for the mean electrostatic potential \bar{V} and its root mean square deviation ΔV_{rms} . We first consider the process of electron beam excitation of optical line radiation from neutral gas atoms. We let

$$n_a = \text{neutral atom density (cm}^{-3}\text{)}$$

$$n_b = \text{electron beam density (cm}^{-3}\text{)}$$

$$n_e = \text{plasma electron density (cm}^{-3}\text{)}$$

$$\langle \sigma v \rangle_b = \text{beam-atom excitation rate (cm}^3\text{/sec)}$$

$$\langle \sigma v \rangle_e = \text{plasma electron-atom excitation rate (cm}^3\text{/sec)}$$

$$\Delta_b = \text{beam-neutral interaction volume (cm}^3\text{)}$$

$$\Delta_e = \text{plasma electron-neutral interaction volume (cm}^3\text{)}$$

Roughly, we estimate (see Fig. 9) that

$$\Delta_b = \pi \tau_b^2 l ,$$

and

$$\Delta_e = 4\tau_b \tau_e l ,$$

where τ_b and τ_e are respectively the beam and plasma radii, and l is the interaction length. Then the photon generation rates for the beam and for the plasma electrons are, respectively,

$$R_b = n_a n_b \langle \sigma v \rangle_b \Delta_b , \quad (\text{photons/sec}) \quad (12)$$

$$R_e = n_a n_e \langle \sigma v \rangle_e \Delta_e , \quad (\text{photons/sec})$$

Now we let

f = beam density modulation frequency (Hz),

Ω = solid angle seen by the optics (steradians),

J = number of sample intervals per modulation period,

M = number of modulation cycles.

The observation time interval; i.e., the time resolution of the measurement, is

$$T = M / f$$

We have divided each modulation period $\tau = 1/f$ into J equal subintervals $\Delta t = \tau/J$. There are thus three time scales: Δt , τ and T .

During a period τ , we observe within each subinterval Δt

$$N_b = \eta R_b \frac{\Omega}{4\pi} \Delta t \quad (\text{photons}) \quad (14)$$

$$N_g = \eta R_g \frac{\Omega}{4\pi} \Delta t \quad (\text{photons}) \quad (15)$$

where $\eta < 1$ is the detector efficiency. We consider N_b as the "signal" and N_g as the "noise." We expect N_b to oscillate at frequency f , while N_g will be steady (dc), with fluctuations due to photon counting statistics. The fluctuations in N_g must be considered because N_b is very small compared to N_g (Note that $n_b \ll n_g$ and $\Delta_b < \Delta_g$). We must use averaging techniques to increase the signal-to-noise ratio of the measurement. Since N_g has a large dc component, we use a baseline subtraction technique, in which samples of the detector output taken without the beam (at some submultiple frequency synchronized to the beam modulation frequency) are alternately subtracted from the samples of the detector output taken with the beam (see Fig. 10). In this manner, the photon baseline for the noise is subtracted, leaving only its fluctuation level. This is a

standard technique performed using boxcar integrators (analog) or transient digitizers (digital).

Taking M samples for each subinterval j (one sample during each modulation period as shown in Fig. 10), we obtain the rms fluctuation level (noise)

$$F_{rms} = (MN_g)^{1/2} \quad (\text{photons}) \quad (16)$$

The signal is present for half the samples, yielding

$$S_j = \frac{1}{2} M N_b(t_j) \quad (\text{photons}) , \quad (17)$$

where t_j (modulo τ) is the subinterval time. Since $N_b \ll N_g$, the fluctuations in S_j are not important. The signal-to-noise ratio is defined as

$$S_j / F = \frac{1}{2} \frac{N_b}{N_g^{1/2}} M^{1/2} , \quad (18)$$

and increases as the square root of the number of samples taken. The output signal from the detector, after averaging, is the set of J values

$$P_j = S_j + F_j \quad (\text{photons}) , \quad (19)$$

where F_j is the number of noise photons in the j th subinterval.

We now determine the phase φ from the values of P_j , and estimate the rms phase uncertainty $(\Delta\varphi)_{rms}$. For simplicity we assume that the signal, uncorrupted by noise, has the form

$$S(t) = S_0 \sin(\omega t + \varphi_0) , \quad (20)$$

where $\omega = 2\pi f$, and S_0 and φ_0 are the amplitude and phase to be determined. (It is easy to add a constant term to S if required).

To determine the "best fit" values of S_0 and φ_0 , we minimize the mean squared error

$$e = \sum_{j=1}^J (S(t_j) - P_j)^2 \Delta t \quad (21)$$

Setting $\partial e / \partial \varphi_0 = 0$ and $\partial e / \partial S_0 = 0$, we obtain the two equations

$$\sum_j P_j \cos(\omega t_j + \bar{\varphi}) = 0 \quad (22)$$

$$\bar{S} = \frac{2}{J} \sum_j P_j \sin(\omega t_j + \bar{\varphi}) \quad (23)$$

Equation (22) determines the "best fit" phase $\bar{\varphi}$, and (23) yields the "best fit" amplitude \bar{S} .

The uncertainty in $\bar{\varphi}$ can be found by inserting (20) into (22):

$$\sum_j S_0 \sin(\omega t_j + \varphi_0) \cos(\omega t_j + \bar{\varphi}) + \sum_j F_j \cos(\omega t_j + \bar{\varphi}) = 0 \quad (24)$$

We assume that $\bar{\varphi}$ is close to φ_0 and that the F_j 's are small. We thus put $\bar{\varphi} = \varphi_0$ in the second term in (24), and put

$$\bar{\varphi} = \varphi_0 + \Delta\varphi ; \Delta\varphi \ll 2\pi$$

in the first term. We then obtain the relation

$$S_0 \frac{J}{2} \Delta\varphi = \sum_j F_j \cos(\omega t_j + \varphi_0) \quad (25)$$

Recall that the F_j are Gaussian-distributed random variables, having $\overline{F_j} = 0$ and $\overline{F_j^2} = F_{rms}^2$.

Averaging over this distribution, we obtain $\overline{\Delta\varphi} = 0$ and

$$\overline{(\Delta\varphi)^2} = (\Delta\varphi_{rms})^2 = \frac{2}{J} \frac{F_{rms}^2}{S_0^2} \quad (26)$$

Using (12)-(17), we obtain

$$(\Delta\varphi_{rms})^2 = \frac{8}{N_T} \frac{n_s}{n_{bmax}} \frac{\langle \sigma v \rangle_s}{\langle \sigma v \rangle_b} \frac{\Delta_s}{\Delta_b} \quad (27)$$

where

$$N_T = \eta \frac{\Omega}{4\pi} n_a n_{bmax} \langle \sigma v \rangle_b \Delta_b T \quad (28)$$

is the total number of beam photons that would be detected during a time interval T if the beam density was n_{bmax} during the entire interval. As expected, we note that $\Delta\varphi_{rms}$ depends only on the averaging time T , and not on τ or Δt .

We now relate the mean potential \bar{V} and its rms deviation ΔV_{rms} to the mean phase $\bar{\varphi}$ and its rms deviation $\Delta\varphi_{rms}$. The phase is given in terms of the potential by the equation

$$\varphi(x) = \omega t(x) = \omega \left(\frac{m}{2e} \right)^{1/2} \int^x dx' [V(x')]^{-1/2} , \quad (29)$$

where $V(x)$ is the potential with respect to the electron beam cathode. Solving for V , we obtain

$$V(x) = \frac{m \omega^2}{2e} [\varphi'(x)]^{-2} , \quad (30)$$

where $\varphi' = d\varphi/dx$.

We use the values of φ obtained at two axial locations (see Fig. 1) to determine φ' :

$$\varphi' = \frac{\varphi_2 - \varphi_1}{L} , \quad (31)$$

where L is the axial separation. We note that φ' has the mean

$$\bar{\varphi}' = \frac{\bar{\varphi}_2 - \bar{\varphi}_1}{L} \quad (32)$$

and the rms deviation

$$\Delta\varphi'_{rms} = \frac{\sqrt{2}\Delta\varphi_{rms}}{L} . \quad (33)$$

Thus V has the mean

$$\bar{V} = \frac{m\omega^2}{2e(\bar{\varphi}')^2} \quad (34)$$

and the rms deviation

$$\Delta V_{rms} = \frac{m\omega^2}{e(\bar{\varphi}')^3} \Delta\varphi_{rms} \quad (35)$$

Inserting (33) and (34) into (35), we obtain

$$\begin{aligned} \Delta V_{rms} &= \frac{4}{\omega} \left(\frac{e}{m} \right)^{1/2} \bar{V}^{3/2} \frac{\Delta\varphi_{rms}}{L} \\ &= A_v \frac{\bar{V}^{3/2}}{fL} \Delta\varphi_{rms} \end{aligned} \quad (36)$$

where $A_v = 2.7 \times 10^5 \text{ m/V}^{1/2}\text{-sec}$.

We want to minimize ΔV_{rms} since we cannot distinguish two measurements of \bar{V} that differ by ΔV_{rms} or less. We therefore examine the scaling of ΔV_{rms} with the system parameters. Before doing this, we eliminate the beam density as a parameter in favor of the beam perveance K by writing

$$I_b = en_b v_b \pi r_b^2 = KV_b^{3/2} \quad (37)$$

which yields

$$n_b = \frac{1}{e} \left(\frac{m}{2e} \right)^{1/2} \frac{KV_b}{\pi r_b^2} \quad (38)$$

Inserting (38) into (27) and (28), we obtain

$$(\Delta\varphi_{rms})^2 = \frac{32}{\eta \frac{\Omega}{4\pi} \frac{m}{2e^3} K^2 \langle \sigma v \rangle_b l T} \frac{n_s}{n_a} \frac{\langle \sigma v \rangle_s}{\langle \sigma v \rangle_b} \frac{\tau_b \tau_s}{V_b^2} \quad (39)$$

Inserting (39) into (36) and setting $\bar{V} \approx V_b$, we obtain the final result

$$(\Delta V_{rms})^2 = \frac{1024e^4}{\pi m^2} \frac{1}{f^2 K^2 \eta \Omega} \frac{n_s}{n_a} \frac{\langle \sigma v \rangle_s}{\langle \sigma v \rangle_b} \frac{\tau_b \tau_s}{LL^2} \frac{V_b}{\langle \sigma v \rangle_b T} \quad (40)$$

For design of the electron beam probe diagnostic system, we should therefore choose

$$f, K, \eta, \Omega, l, L, \text{ and } T$$

as large as possible, and choose

$$V_0 \text{ and } \tau_0$$

as small as possible (we assume here that $\langle \sigma v \rangle$ is roughly independent of v).

2. Numerical estimates

The modulation frequency f will be limited by the transition time for the line radiation of the gas atoms observed, and by the wavelength v_0/f of the beam bunches. For the Balmer lines of hydrogen, the transition rate is ≈ 64 MHz; for Lyman α , the rate and cross sections are higher: ≈ 164 MHz. However, the optics in the vacuum uv are more difficult. We thus choose

$$f \approx 40\text{MHz.}$$

For the v_0 we will choose, this yields a reasonable beam wavelength.

We consider the use of a magnetron injection gun. Such a gun with $K \approx 6 \times 10^{-6}$ has been operated in TMX-U. We choose a reasonable value

$$K \approx 10^{-5} \quad A/V^{3/2} .$$

We choose a detection efficiency

$$\eta \approx 0.3 .$$

A 6" diameter lens placed 30" from the plasma is presently used for the Thompson scattering diagnostic in TMX-U. We assume that the same solid angle can be chosen for the electron beam probe;

$$\Omega = .031 \quad \text{steradians .}$$

We choose an interaction length and an axial separation between measurement stations

$$l = L = 30 \text{ cm.}$$

We choose an averaging time

$$T = 10^{-2} \text{ sec.}$$

These later choices specify the space and time resolution of the measurement.

The beam voltage must be of the order of the typical potentials in the experiment. A reasonable lower limit might be

$$V_b \approx 2 \text{ kV.}$$

The beam diameter is limited by the observing optics, magnetic field line wandering etc. A reasonable lower limit is

$$r_b = 1 \text{ cm.}$$

With these parameters, the beam velocity is

$$v_b = 2.7 \times 10^9 \text{ cm/sec.}$$

the beam current is

$$I_b = 0.89 \text{ A,}$$

the beam density is

$$n_b = 6.6 \times 10^8 \text{ cm}^{-3},$$

and the beam interaction volume is

$$\Delta_b \approx 94 \text{ cm}^3.$$

We estimate the plasma parameters as follows: A 20 cm parabolic radius leads to an average plasma radius

$$r_p \approx 13 \text{ cm,}$$

and an interaction volume

$$\Delta_p = 1560 \text{ cm}^3.$$

The plasma electron density is taken to be

$$n_p \approx 5 \times 10^{11} \text{ cm}^{-3}.$$

The plasma electron and beam excitation cross sections are estimated as follows: The Lyman α cross section for 250 eV plasma electrons is $0.34 \times 10^{-16} \text{ cm}^2$. We estimate the cross section for production of radiation above 2200 Å to be roughly half this value:

$$\sigma_p \approx 0.17 \times 10^{-16} \text{ cm}^2.$$

For a 2 kV beam, we estimate

$$\sigma_b \approx .04 \times 10^{-16} \text{ cm}^2.$$

The plasma-electron excitation rate is then

$$\langle \sigma v \rangle_e \approx 1.1 \times 10^{-8} \text{ cm}^3/\text{sec}.$$

and the beam excitation rate is

$$\langle \sigma v \rangle_b \approx 1.1 \times 10^{-8} \text{ cm}^3/\text{sec}.$$

The neutral pressure is a difficult parameter to estimate. We adapt the estimate

$$p_a \approx 5 \times 10^{-7} \text{ torr} ,$$

such that the neutral density is

$$n_a \approx 1.7 \times 10^{10} \text{ cm}^{-3}.$$

We note in passing that the neutral atom density in a fast neutral beam is of order 10^{10} cm^{-3} . Therefore, if the neutral pressure is much below 2×10^{-7} torr, then a neutral beam may be injected into the interaction volume to achieve a density of order 10^{10} cm^{-3} .

For the above parameters, we have the following estimates using (12) and (13):

$$R_b \approx 1.2 \times 10^{13} \text{ (photons/sec)}$$

$$R_e \approx 1.5 \times 10^{17} \text{ (photons/sec)}$$

$$M = 4 \times 10^5 \text{ (number of cycles averaged)}$$

For $J = 10$ subintervals, we find using (14) and (15) that

$$N_{bmax} \approx 22 \quad (\text{photons})$$

$$N_e \approx 2.8 \times 10^6 \quad (\text{photons}) .$$

Using (16), and (17), we obtain

$$F_{rms} \approx 3.3 \times 10^5 \quad (\text{noise photons/subinterval})$$

$$S_{jmax} \approx 4.4 \times 10^6 \quad (\text{signal photons/subinterval}) .$$

Using (28), we obtain

$$N_T = 8.6 \times 10^7 \quad (\text{photons}) ,$$

and, using (27), we obtain

$$\Delta\phi_{rms} = .034 \quad \text{radians} .$$

Finally, using (40) we obtain the rms potential deviation

$$\Delta V_{rms} \approx 67 \text{ V} .$$

If we are willing to accept a potential uncertainty a factor of $\sqrt{10}$ larger (~ 210 V), then we can, for example, reduce the solid angle or the neutral density by a factor of 10 or increase the plasma electron density by a factor of 10. We conclude that the measurement is feasible on TMX-U, at least for certain operating regimes. More careful theoretical and numerical studies should be done to refine these estimates. Experimental work should be initiated to explore the physics issues and to determine the limitations of the method.

D. Remote Detection Using Plasma Ion Targets

1. Measurement technique

We detect x-rays at 2-10 keV. This method has also been suggested by Klinkowstein.¹ There is no limit on transition rate as for an optical line, so we choose $f = \nu_b / \lambda$ or

$$f^2 = \frac{2e}{m} \frac{V_b}{\lambda^2} \quad (41)$$

and let $l = L = \lambda/2$. The target density n_a in (40) is replaced by $Z^2 n_i$, where n_i is the ion density and Z is the effective charge.

The rate constant $\langle \sigma \nu \rangle_b$ for x-ray bremsstrahlung photons is estimated as follows: the total power radiated per beam electron is²

$$P_x = \frac{e^2 (Ze)^4 n_i}{24 \pi \epsilon_0^3 c^3 m h} \nu_b \quad (\text{watts}) ,$$

where h is Planck's constant.

The energy spectrum of the power is roughly flat up to the energy E_b of the incident electron and falls precipitously thereafter. Assuming the detection of x-rays in the range E_{\min} to E_b , the number of photons emitted/sec-electron is

$$\int_{E_{\min}}^{E_b} \frac{1}{E} \frac{P_x}{E_b} dE = \frac{P_x}{E_b} \ln \frac{E_b}{E_{\min}} .$$

The rate constant is then

$$\begin{aligned} \langle \sigma \nu \rangle_b &= \frac{e^2 (Ze)^4}{12 \pi \epsilon_0^3 m^2 c^4 h} \frac{c}{\nu_b} \ln \frac{E_b}{E_{\min}} \\ &= 1.44 \times 10^{-22} Z^2 \frac{c}{\nu_b} \ln \frac{E_b}{E_{\min}} \quad (\text{m}^3 / \text{sec}) . \end{aligned}$$

Using $V_b = \frac{1}{2} m \nu_b^2 / e$, we obtain

$$\langle \sigma \nu \rangle_b = C_b Z^2 V_b^{-1/2} \ln(V_b / V_{\min}) \quad (42)$$

where

$$C_b = 7.3 \times 10^{-20} \text{ (m}^3\text{-V}^{1/2}\text{/sec) .}$$

There are three significant noise sources in the detection of beam-produced x-ray photons. Two possible background noise sources are plasma, hot-electron-produced x-ray photons, and plasma, cold-electron-produced photons.

As will be shown, these background noise sources can be made small in certain regions of a tandem mirror by proper choice of beam energy. However, the basic reaction rate (42) is very small, such that statistical fluctuations in the signal (beam-produced) photons may be dominant. We can estimate the contribution of signal photon fluctuations to the rms phase uncertainty as follows: For the signal photons $S(t)$ given by (20), we have an rms fluctuation

$$F_{rms} \approx (S_0/2)^{1/2} \text{ (photons) .} \quad (43)$$

The rms uncertainty in the phase $\bar{\varphi}$ due to this source is, using (26),

$$(\Delta\varphi_{rms})^2 = \frac{1}{S_0 J} = \frac{1}{N_T} , \quad (44)$$

where N_T is the total number of beam produced photons that would be detected during the time interval T if the beam density was $n_{bmax}(S(t) = S_0)$ during the entire interval.

Referring to (27), we see that (44) corresponds to an additional noise photon rate

$$\frac{1}{8} n_{bmax} \langle \sigma v \rangle_b \Delta_b \text{ (m}^3\text{/sec)} \quad (45)$$

in the numerator of (27).

We consider now the two external noise sources: plasma hot electrons having $T_h \gg V_b$, and plasma cold electrons having $T_c \gg V_b$.

For Maxwellian hot electrons, we have

$$f_h = \frac{n_h}{(2\pi)^{3/2} v_h^3} \exp\left[-\frac{mv_h^2}{2k T_h}\right].$$

We estimate the production of x-rays having energies below V_b as arising from a sphere in velocity space of radius v_b . This yields

$$n_h \langle \sigma v \rangle_h \Delta_e \approx n_h \langle \sigma v \rangle_b \left(\frac{V_b}{T_h}\right)^{3/2} \Delta_e. \quad (46)$$

For cold plasma electrons at temperature $T_c \ll V_b$, the production of x-rays having energies near or somewhat below V_b arises from the Maxwellian tail having $v > v_b$. This yields

$$n_c \langle \sigma v \rangle_c \Delta_e \approx n_c \langle \sigma v \rangle_b \frac{V_b}{T_c} e^{-V_b/T_c} \Delta_e. \quad (47)$$

Using (41) and (42) in (40), and replacing the noise rate $n_c \langle \sigma v \rangle_c \Delta_e$ in (40) by the sum of (45), (46), and (47) we obtain the scaling law

$$\begin{aligned} (\Delta V_{rms})^2 = & \frac{5096e^3}{\pi n C_b} \frac{\tau_b \tau_e V_b^{1/2}}{K^2 \eta \Omega \lambda T} \\ & \frac{n_h \left(\frac{V_b}{T_h}\right)^{3/2} + n_c \left(\frac{V_b}{T_c}\right) e^{-V_b/T_c} + n_{bmax} \frac{\pi \tau_b}{32 \tau_e}}{Z^2 n_i \ln(V_b / V_{min})}. \end{aligned} \quad (48)$$

2. Numerical estimates

We first choose all parameters as before ($\lambda/2 = l = 30$ cm; $f = 45$ MHz), except that we take

$$\Omega \approx 10^{-3},$$

since x-rays cannot be focused. For an optimistic case, we ignore the plasma electron noise ($n_h \approx n_c \approx 0$ in the noise term) and choose

$$Z \approx 1.$$

$$n_i \approx 5 \times 10^{11} \text{ cm}^{-3}$$

$$V_b / V_{\min} \approx 2.72$$

Then

$$\langle \sigma v \rangle_b \approx 1.6 \times 10^{-15} \text{ cm}^3 / \text{sec.}$$

$$R_b \approx 4.9 \times 10^7 \text{ photons/sec.}$$

$$M \approx 4.5 \times 10^5 .$$

Again for $J = 10$ subintervals, using (14), we obtain

$$N_{bmax} \approx 2.6 \times 10^{-6} \text{ photons .}$$

Using (17) and (43), we obtain

$$S_0 = S_{jmax} \approx .59 \text{ (signal photons/subinterval)}$$

$$F_{rms} \approx .54 \text{ (noise photons/subinterval)}$$

Using (28) with n_x replaced by n_i , we obtain

$$N_T \approx 11.7 \text{ photons ,}$$

and using (44), we obtain

$$\Delta\phi_{rms} \approx .29 \text{ radians .}$$

Finally, using (36), we obtain the rms potential deviation

$$\Delta V_{rms} \approx 520 \text{ V .}$$

This uncertainty is too large, and thus the measurement is not feasible for this (low) ion density. We see from (48) that increasing n_i by a factor of ten,

$$n_i = 5 \times 10^{12} \text{ cm}^{-3} ,$$

will decrease the uncertainty to

$$\Delta V_{rms} \approx 164 V .$$

However, the measurement technique looks marginal except at the highest ion densities. It may be more attractive in MFTF-B, since both n_i and ΔV_{rms} may be considerably larger than in TMX-U.

E. Remote Detection Using Beam Magnetic Fields

1. Basic feasibility

We consider the use of a magnetic field detection coil located near the chamber wall to detect the modulated electron beam current. The basic concept of the measurement is shown in Fig. 11, and follows from ampere's law

$$\nabla \times B = \mu_0 J . \quad (49)$$

For simplicity, we assume a travelling beam modulated at frequency ω with constant velocity v_b and initial phase φ :

$$J = \hat{x} J_0 \sin[\omega(t - \frac{x}{v_b}) + \varphi]$$

Substituting this expression into (49), in the \hat{x} direction, we obtain

$$\frac{1}{\rho} \frac{\partial(\rho B_\theta)}{\partial \rho} = \mu_0 J .$$

If we multiply by $\int_0^a 2\pi\rho d\rho$ and integrate both sides, we have

$$B_\theta = \frac{\mu_0 I_0}{2\pi a} \sin[\omega(t - \frac{x}{v_b}) + \varphi] . \quad (50)$$

For the Rogowski coil, the voltage signal produced by dB_θ/dt is

$$v_L(t) = N \frac{d\Phi_L}{dt} = NA_L \frac{\mu_0 I_0}{2\pi a} \omega \cos [\omega(t - \frac{x}{v_b}) + \varphi] \quad (51)$$

where N is the number of turns, A_L is the cross sectional area of a single turn, and a is the radius of the coil. If we choose:

$$N = 10 ,$$

$$I_0 = 10 \text{ A} ,$$

$$\omega = 2\pi \times 2 \times 10^7 \text{ rad./sec.} ,$$

and

$$a = 0.30 \text{ m} ,$$

then

$$V_0 = NA_L \frac{\mu_0 I_0}{2\pi a} \omega = 7.4 \text{ volts.}$$

This a very large signal and demonstrates the basic feasibility of the technique.

Rather than using a Rogowski coil around the entire plasma, we can insert a smaller, B_θ -detecting coil (not a Rogowski coil) near the chamber wall (see Fig. 11). The above analysis holds for this coil configuration also.

2. Plasma neutralization

A critical issue that must be examined is shielding of the electron beam current-induced magnetic field. In an isotropic plasma, the dispersion equation is

$$k_x^2 + k_\perp^2 = \frac{\omega^2}{c^2} \left(1 - \frac{\omega_p^2}{\omega^2}\right) \approx -\frac{\omega_p^2}{c^2} ,$$

where k_x and k_\perp are the parallel and perpendicular wavenumbers excited by the beam current, and $k_p^{-1} = c/\omega_p$ is the collisionless skin depth. For $n_e \approx 10^{12} \text{ cm}^{-3}$, $k_p^{-1} \approx 0.5 \text{ cm}$. For $k_x \ll k_p$, we find $k_\perp \approx ik_p$, such that the magnetic field decays radially from the beam with a characteristic decay distance k_p^{-1} that is very short. Fortunately, the presence of a strong magnetic field (and, possibly, finite resistivity) modifies this result. For $\omega \ll \omega_{ci}$, Alfvén

waves can propagate, and these carry the beam current-induced magnetic field to the outer radius of the plasma, where the field can be detected using a loop antenna. The strength of the magnetic field at the antenna must be determined by solving the appropriate boundary value problem. This theoretical study bears crucially on the feasibility of magnetic detection of the electron beam phase, since it determines the observed signal strength for a given beam current level. In addition, experimental studies of beam current-induced magnetic fields should be performed to verify the theoretical models.

3. Spatial resolution and time response

For a modulated electron beam propagating in a vacuum, the axial spatial resolution L for detection of the beam phase is limited by the quasistatic (Laplace equation) solution to

$$L \sim a$$

where a is the radial location of the loop antenna: $a \gtrsim r_p$, the plasma radius. This is an acceptable axial spatial resolution in tandem mirrors. However, the effect of the plasma dispersion in modifying this result must be studied.

The response time of a coil is limited by the coil inductance L , and the capacitance C and resistance R seen at the coil terminals. First considering resistive effects, we have the circuit shown in Fig. 12a, with time constant

$$\tau = L/R \quad (52)$$

The self-inductance of an N -turn cylindrical coil of radius r_0 and length l is³

$$L = K \mu_0 N^2 \frac{\pi r_0^2}{l},$$

where K is given in the table below.

τ_0/l	0	.2	.6	1.0	2.0	4.0	10.0
K	1	.85	.65	.53	.37	.24	.12

There are two possible operating regimes for τ : (a) $\tau \ll 1/f = 2\pi/\omega$ and (b) $\tau \gg 1/f$. In the short time constant regime (a), the coil is capable of passing the modulation signal, and the voltage output scales as

$$v(t) \sim \frac{dB_y}{dt} \sim \frac{di_b}{dt} \sim \omega i_b(t) .$$

This regime may be preferable because of relative immunity to low frequency, magnetic field induced noise. For this regime we require L small and R large. Using the parameters specified in Sec. E1 again, one can calculate the inductance assuming that $R/l \approx 2$:

$$L \approx 5 \mu\text{H} .$$

In order to obtain a small τ , we choose $R = 500 \Omega$, so that

$$\tau = L/R = .01 \mu\text{sec.} \ll 1/f = .05 \mu\text{sec.}$$

The total capacitance C (internal and external) seen by the coil also limits the frequency response of the coil. We require (see Fig. 12b)

$$1/(\omega C) \gg R ,$$

which leads to

$$C \ll 60 \text{ pF} .$$

This is a reasonable design requirement to meet.

In the second regime (b) of operation, the signal is integrated, so that the voltage output scales as

$$v(t) \sim i_b(t) .$$

The signal amplitude is a factor of $\omega\tau$ below that of regime (a) which may be acceptable since the magnetic noise is also reduced. To determine τ we can choose appropriate values of L and R such that $\omega\tau \gg 1$, or we can use an external integrator (Fig. 12c). For the same example as in (a), if we choose $R = 10 \Omega$, we obtain

$$\tau = L/R \approx 0.5 \mu\text{sec} \ll 1/f .$$

This regime is advantageous since the general impedance level is low, thus relaxing the requirements on keeping C low, and gaining immunity against electrostatic pickup at the coil. However, the coil can be well-shielded electrostatically, and thus the impedance level need not be held very low. Further studies must be done to optimize the coil inductance, capacitance and resistance to maximize the signal-to-noise ratio.

Electrostatic shielding is accomplished by surrounding the coil with a grounded metal shell. The magnetic field penetration time through the shell is

$$\tau_s \sim \frac{\mu_0 r_s \delta \sigma}{2}$$

where r_s is the shell radius, δ is the shell thickness (assumed smaller than a skin depth) and σ is the shell conductivity. For stainless steel with $\delta \approx 0.5$ mm, $r_s = 1$ cm, $\tau_s \approx 60 \mu\text{sec} \gg 1/f$. Therefore a slot is necessary in the shell to allow for magnetic field penetration into the loop at the modulation frequency f .

4. Noise sources and bandwidth reduction techniques

The primary source of noise for this technique will be plasma-induced magnetic field fluctuations. The level of these fluctuations is difficult to estimate theoretically, and therefore noise levels must be determined experimentally.

First, a survey of measurements in existing tandem mirrors must be performed. Based on this survey, it may be necessary to perform certain experiments to determine the magnetic field, spectral noise levels in the frequency range of interest. Such a study, along with the study of antenna signal strength in Sec. E3, must be used to optimize the beam modulation frequency.

To increase the signal-to-noise ratio, bandwidth limiting or phase-sensitive detection techniques will probably be required, as described in Secs. C and D. Analog techniques include the use of notch filters, tuned amplifiers, or lock-in amplifiers. The latter (phase-sensitive detection) technique is available in the required frequency range and yields the greatest immunity from noise and filter phase characteristics. Phase-sensitive detection can also be done digitally by post-processing the output voltage collected using transient digitizers, as described in Sec. B.

F. Electron Beam-Plasma Instabilities

For all remote detection techniques, beam-plasma instabilities may lead to dispersion in beam parallel velocity and a reduction in measured signal strength. In addition, beam phase shift may no longer be related simply to variations in plasma potential; i.e., the electron beam may slow down due to beam-plasma interactions.

The problem of a filamentary electron beam propagating along the axis of a plasma-filled waveguide is illustrated in Fig. 13. This problem has been considered previously,^{4,5} and one can apply the results directly. If ω and ω_{pb} are far from ω_{pi} or ω_{ci} , there is no synchronous interaction, and one can, under the assumption $b \ll a$ of a filamentary beam, write⁴

$$(\beta - \beta_0)^2 = \frac{1}{2} \frac{\omega_{pb}^2 b^2 \omega^2}{v_b^4 K_{\perp}} \ln \left(\frac{1}{|q_s b|} \right)$$

where $\beta_0 = \omega / v_b$, and

$$\beta^2 K_{\parallel} + q_e^2 K_{\perp} = 0 .$$

Here β is the longitudinal wavenumber, q_e is the transverse wavenumber, and

$$K_{\parallel} = 1 - \frac{\omega_{pb}^2}{\omega^2}$$

$$K_{\perp} = 1 - \frac{\omega_{pi}^2}{\omega^2 - \omega_{ci}^2} - \frac{\omega_{pe}^2}{\omega^2 - \omega_{ce}^2}$$

are the parallel and perpendicular dielectric tensor components.

We let $b = 0.5$ cm, $n_e = 10^{12}$ cm⁻³, $V_b = 5$ kV, $B_0 = 0.5$ T, $I_b = 10$ A, and $\omega = 2\pi \cdot 20$ MHz = 1.3×10^8 rad/sec. For these parameters, $\beta_0 \approx 3$ m⁻¹, $K_{\perp} \approx -144$ and $K_{\parallel} \approx -2 \times 10^5$, such that we obtain

$$(\beta - \beta_0)^2 \approx -0.13 ,$$

yielding $\text{Im } \beta \approx 0.11$ m⁻¹, or a growth length of 9 m. Thus the system is weakly unstable. At the modulation frequency ω , non-synchronous growth from an initial large amplitude may play an important role in beam velocity diffusion.

Since ω_{pb} is not too far from ω_{pi} , it may be important to estimate the maximum growth rate, which occurs at synchronous interaction. Assuming $\omega \gtrsim \omega_{pi}$, we obtain

$$(\text{Im } \beta)_{\text{max}} \approx \frac{\sqrt{3}}{2} \frac{\omega_{pi}}{v_b} \left(\frac{\omega_{pb}^2}{2\omega_{pe}^2} \right)^{1/3} R_m$$

where

$$R_m^3 = \frac{\pi^2}{4} \frac{b^2}{a^2} \chi_{01} N_0^2 (\chi_{01})$$

and $\chi_{01} = 2.405$ is the first zero of the Bessel function J_0 , and N_0 is the Bessel function of the second kind. Using the same parameters as for non-synchronous interaction, we estimate

$$(\text{Im } \beta)_{\text{max}} \approx 0.4 \text{ m}^{-1}$$

or a growth length of 2.5 m. This is a significant spatial growth rate. Synchronous growth from noise may also be important in beam velocity diffusion.

Assuming that the beam-plasma interaction is fully developed, we expect that the original beam distribution function

$$f_b(v) = \delta(v - v_b)$$

diffuses strongly in velocity space to form a quasilinear plateau:

$$\begin{aligned} f_b(v) &= 1/v_b, \quad v < v_b \\ &= 0, \quad v > v_b. \end{aligned}$$

The phase modulation for this diffused beam has been considered,¹ with the result that the beam density modulation persists, and reaches a quasiequilibrium value for distances $x \gg \beta_0^{-1}$ downstream of the applied beam modulation. Thus a strongly diffused, quasilinear beam can successfully be used for beam time-of-flight measurements. We also note that electron beam, time of flight measurements have been successfully made on the MMX device. However, further studies of this problem must be performed to understand the transition from a monoenergetic to a quasilinear beam distribution and to estimate the timescale for quasilinear beam formulation.

REFERENCES

- ¹R. Klinkowstein, "Electron Beam Potential Diagnostic for Tandem Mirrors," presented at the Joint U.S.-Japanese Workshop on Local Plasma Potential and Magnetic Field Measurements, Sept. 24-25, 1984, Lawrence Livermore National Laboratory, Livermore, CA 94550.
- ²D. J. Rose and M. Clark, Jr., **Plasmas and Controlled Fusion**, J. Wiley, New York (1961) p. 233.
- ³P. Lorrain and D. R. Corson, **Electromagnetic Fields and Waves**, W. H. Freeman, San Francisco, CA (1970), p. 347.
- ⁴M. A. Lieberman, "Ion Oscillations Excited by Electron Beam-Plasma Interaction," Ph.D. Thesis, Department of Electrical Engineering, M.I.T., Cambridge, MA (1966), p. 176.
- ⁵R. J. Briggs, **Electron-Stream Interaction with Plasmas**, M.I.T. Press, Cambridge, MA (1964), p. 97.

FIGURE CAPTIONS

- Fig. 1. Remote sensing for electron beam, time-of-flight measurements to determine the electrostatic potential $V(x)$ in large tandem mirror experiments.
- Fig. 2. Electron beam time-of-flight measurement of thermal barrier potential on the Multiple Mirror Experiment (MMX).
- Fig. 3. Electron beam diagnostic setup on the MMX.
- Fig. 4. Square well model for thermal barrier formation and destruction.
- Fig. 5. A typical time-of-flight measurement for one experimental discharge shot; (a) raw data $\nu_{out}(t)$ vs t , digitized at 100 MHz sampling rate, with every other sample shown; (b) reduced data; showing beam phase delay $\Delta\phi(t)$ vs t , with averaging over 100 rf cycles, yielding 10 μ sec time resolution. The rms deviation is shown as the vertical line. The circles are points whose rms deviations exceed 0.8 radians.
- Fig. 6. Experimental data for the discharge shot of Fig. 5; (a) $Si(Li)$ detector signal showing x-ray pulse heights (keV) vs time t ; (b) Langmuir probe ion saturation current I_{sat}^+ vs t in midplane M_{78} ; (c) interferometer measurement of density n_{67} in the ECRH cell vs t ; (d) electron beam phase delay $\Delta\phi$ vs t .
- Fig. 7. Three-cell, one-dimensional dynamic model of potential barrier formation and destruction in the MMX. Γ_e and Γ_i are electron and ion fluxes respectively; X_i is the ion trapping fraction, and "*" denotes evaluation delayed by an ion transit time.
- Fig. 8. Solution of the dynamic model of Fig. 7 for the data of Fig. 6; (a) normalized barrier potential Φ/T_c vs t ; (b) normalized cold electron density n_{c2}/n_0 vs t in the ECRH cell; (c) normalized ion density n_{i2}/n_0 vs

t in the ECRH cell; (d) phase delay $\Delta\phi$ vs t .

Fig. 9. Definitions of beam and plasma interaction volumes.

Fig. 10. Signal averaging procedure that incorporates a baseline subtraction technique.

Fig. 11. Detection of electron beam current using a Rogowski coil or a B_{θ} -detecting loop.

Fig. 12. Equivalent circuit models for a coil.

Fig. 13. Beam-plasma interaction geometry for a filamentary beam in a plasma filled waveguide; $b \ll a$.

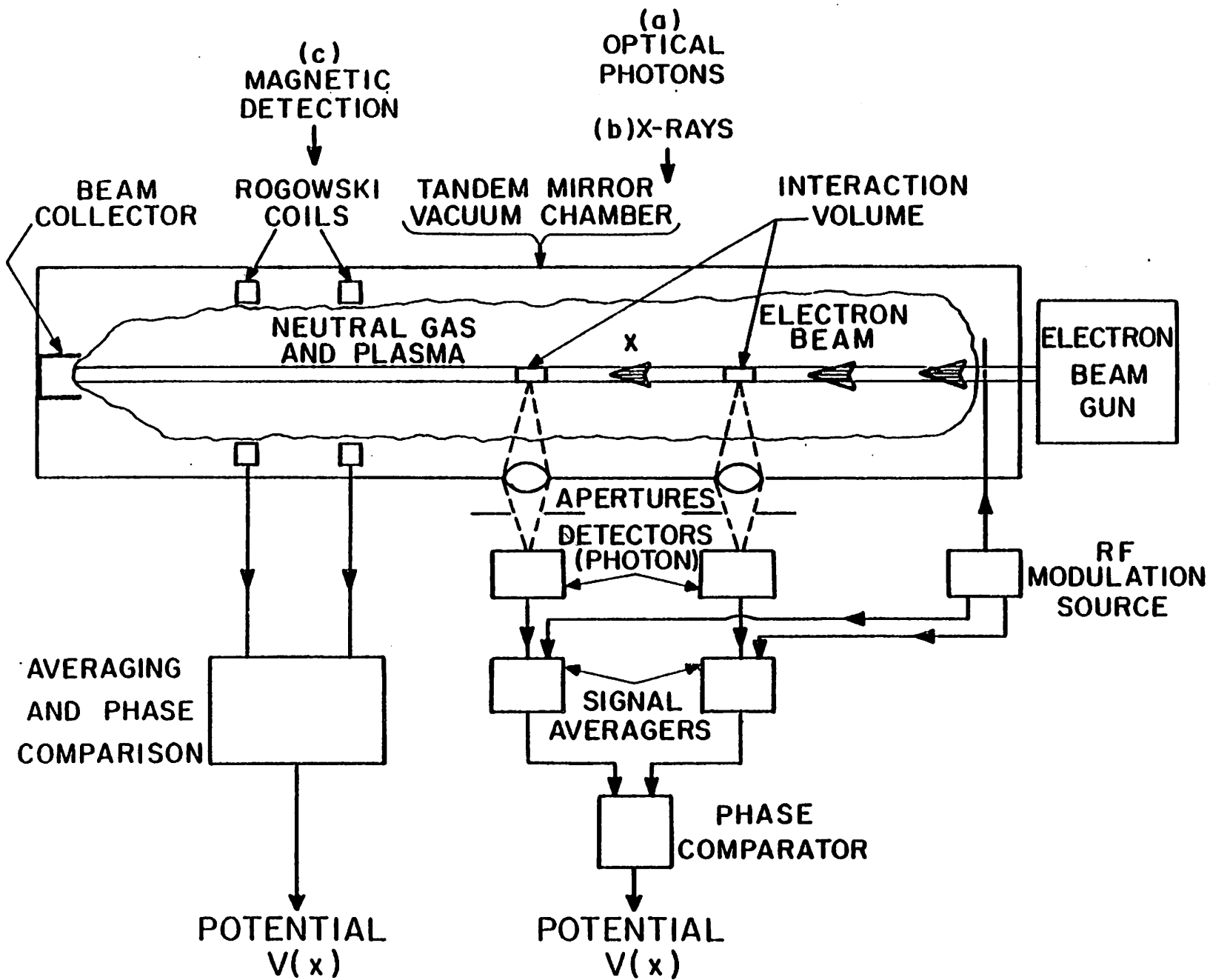


Fig. 1

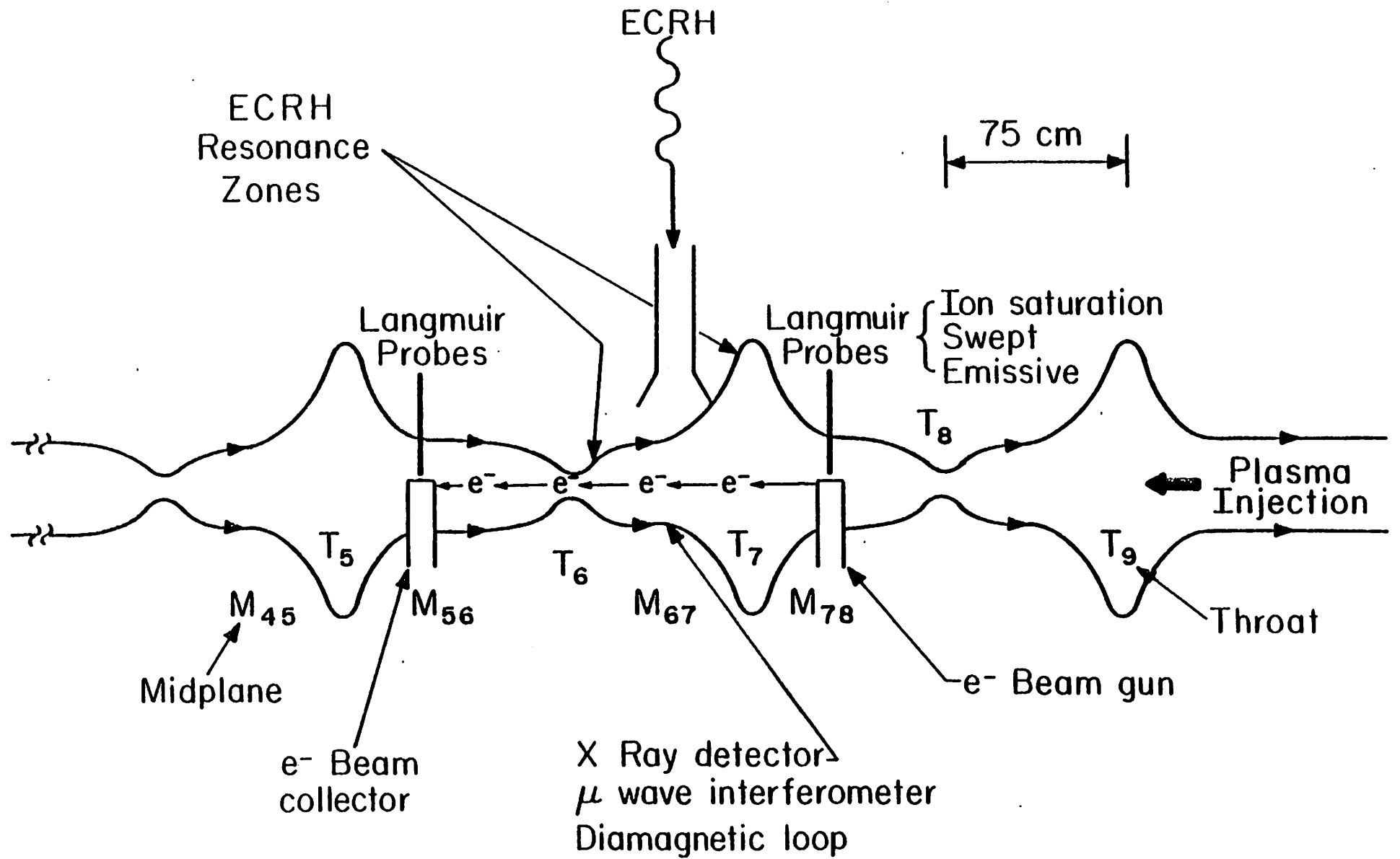


Fig. 2

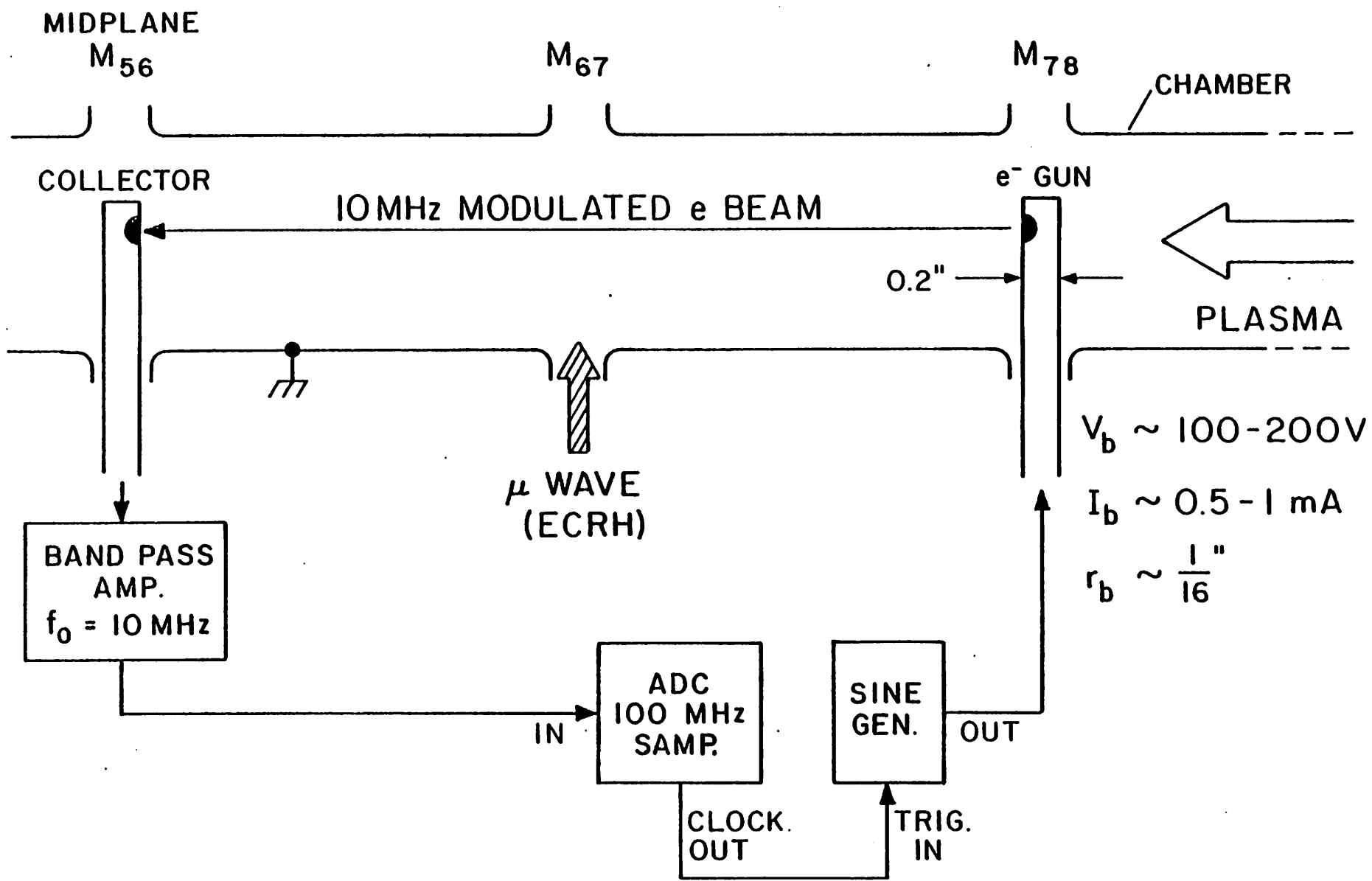


Fig. 3

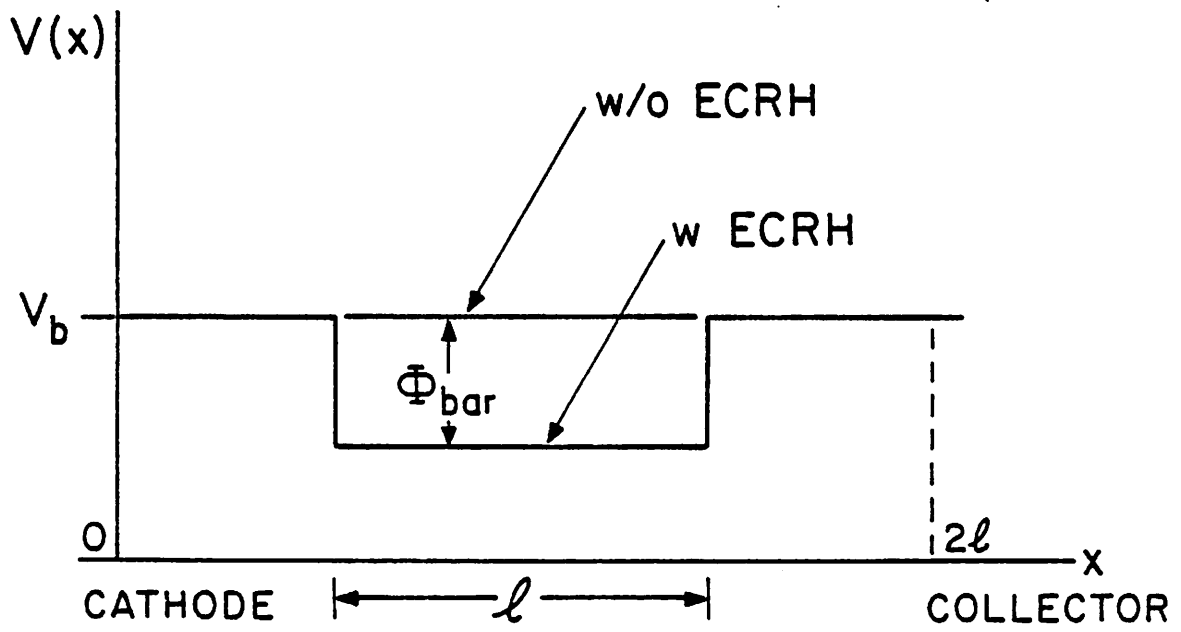


Fig. 4

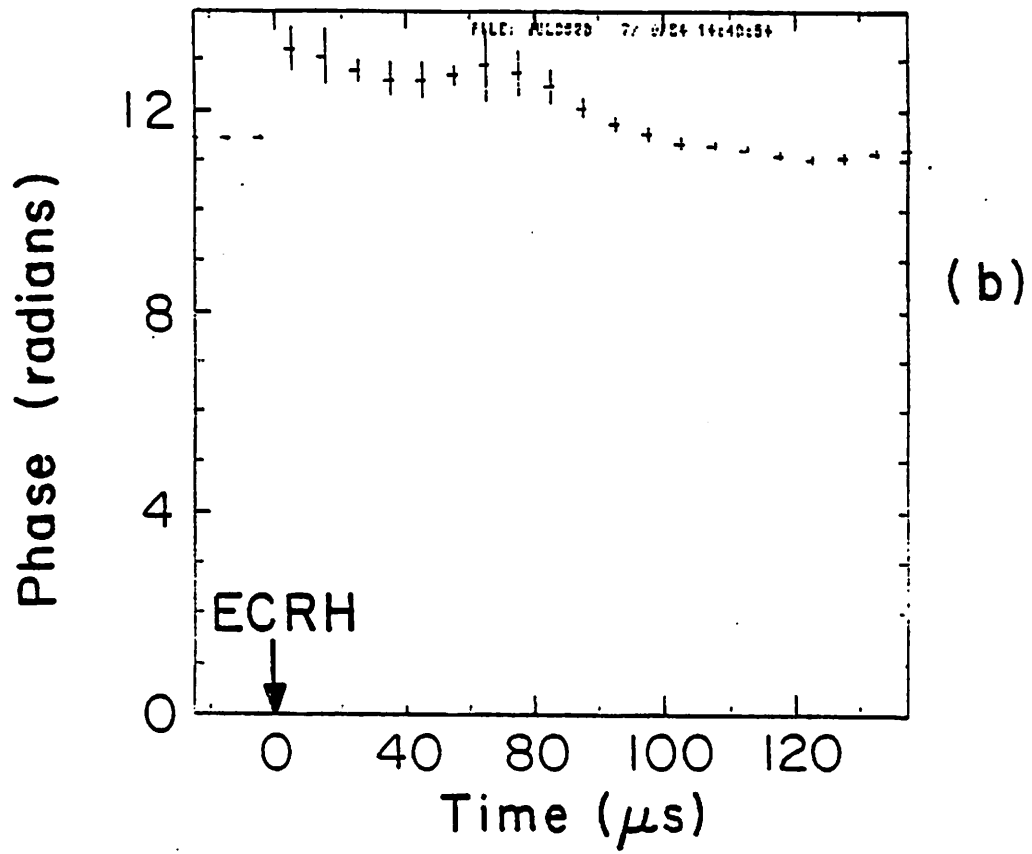
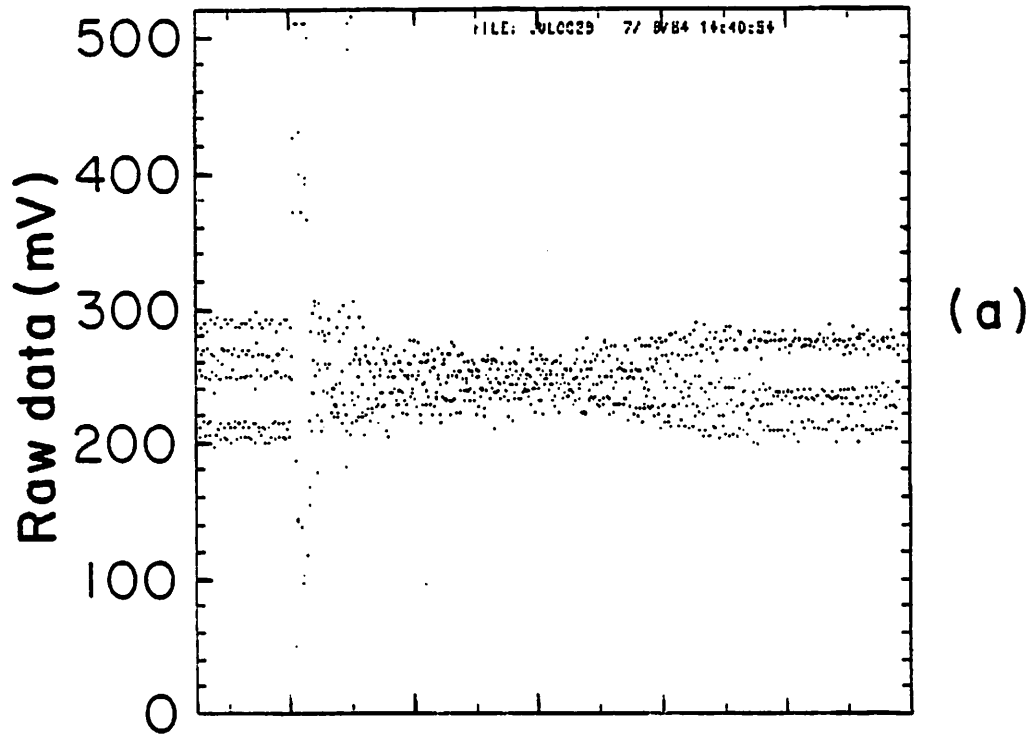


Fig. 5

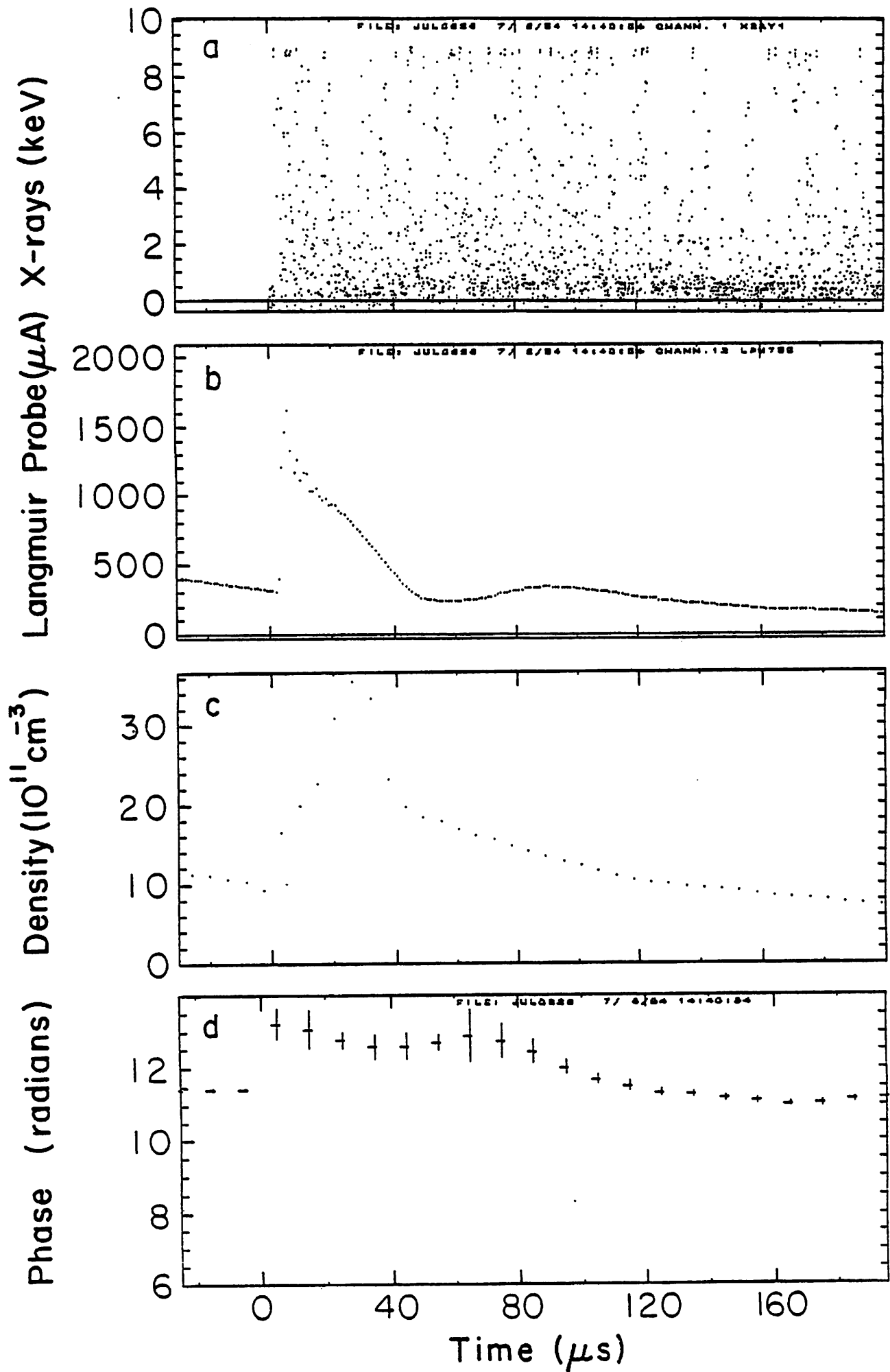


Fig. 6

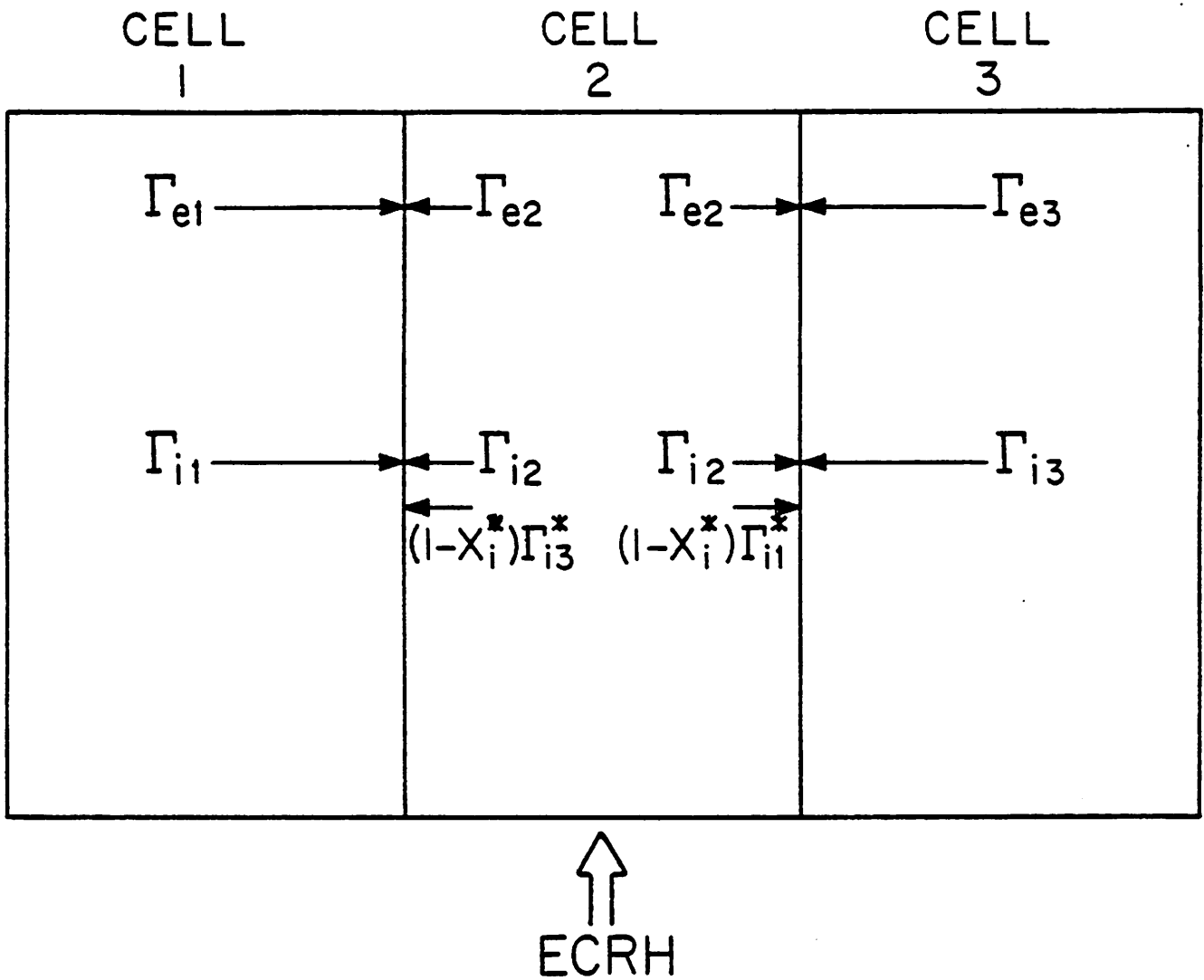


Fig. 7

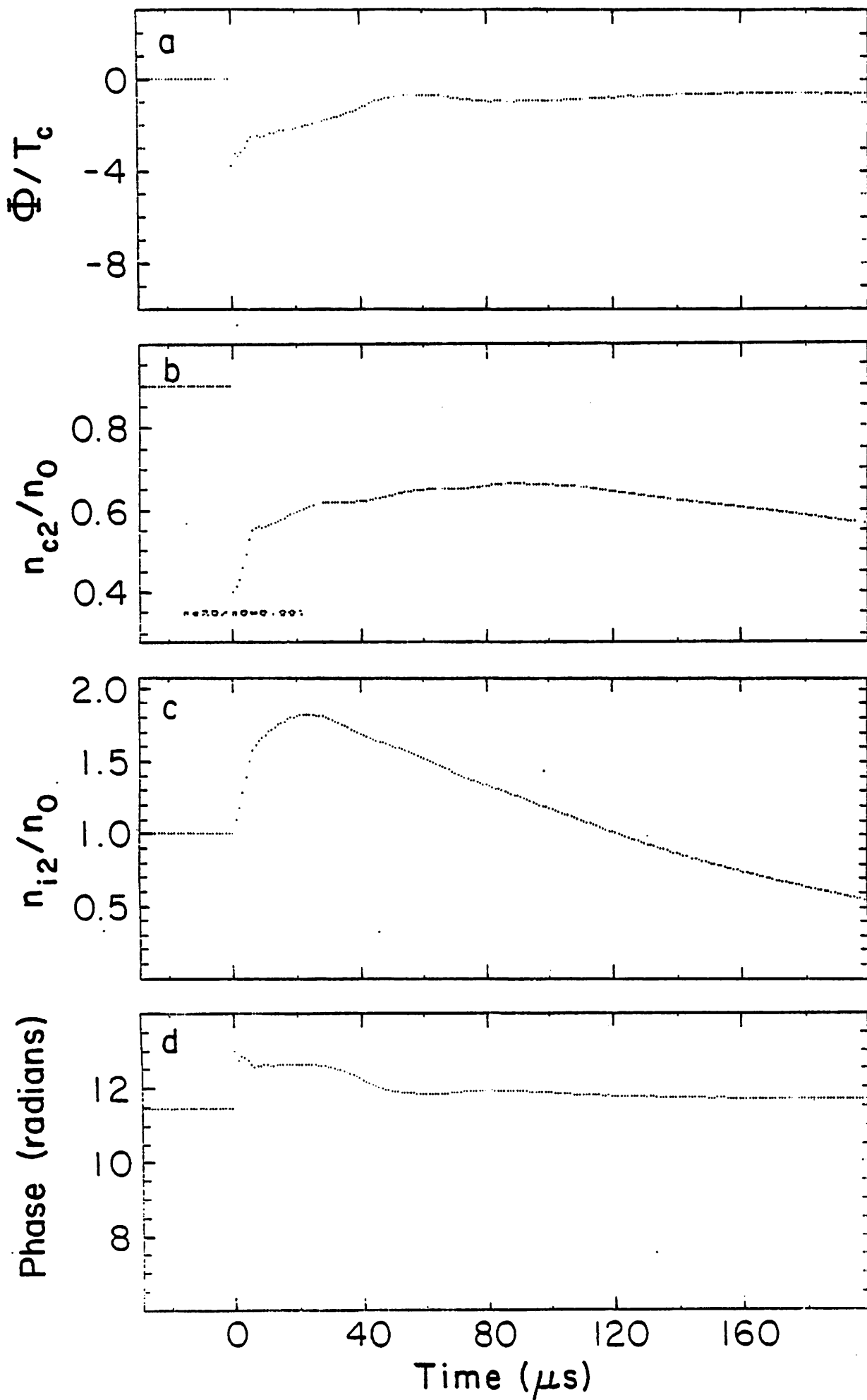


Fig. 8

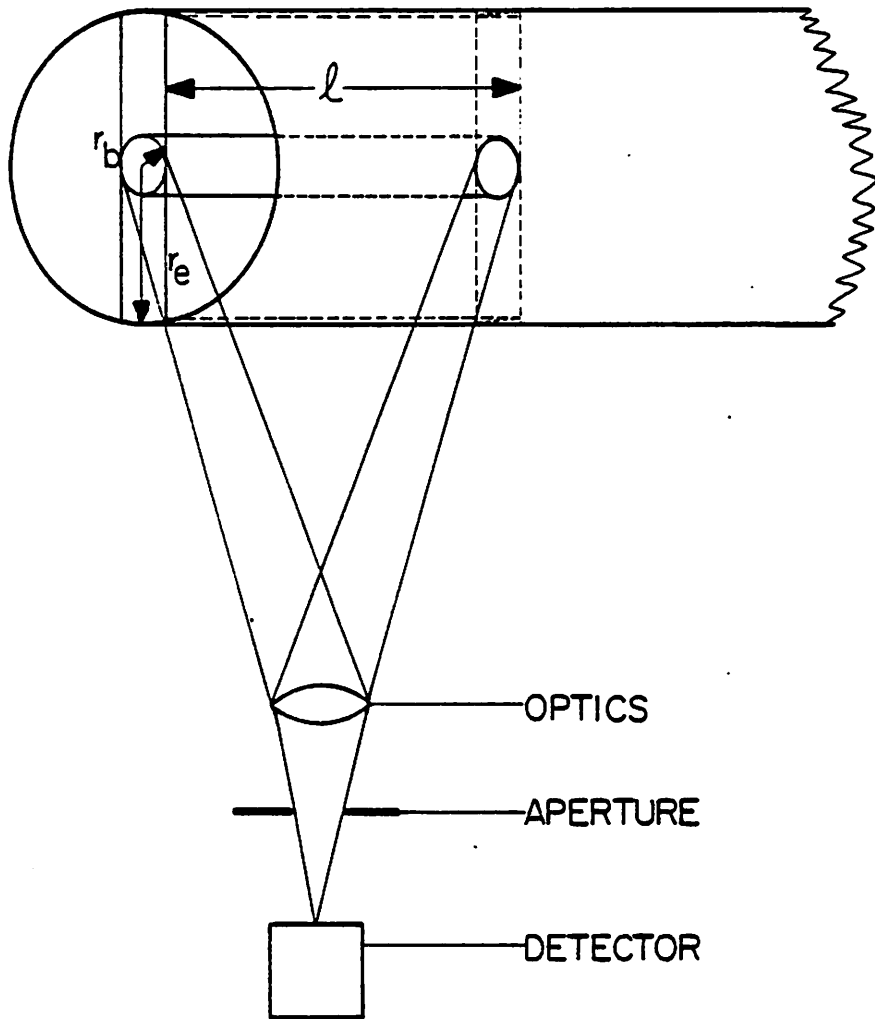


Fig. 9

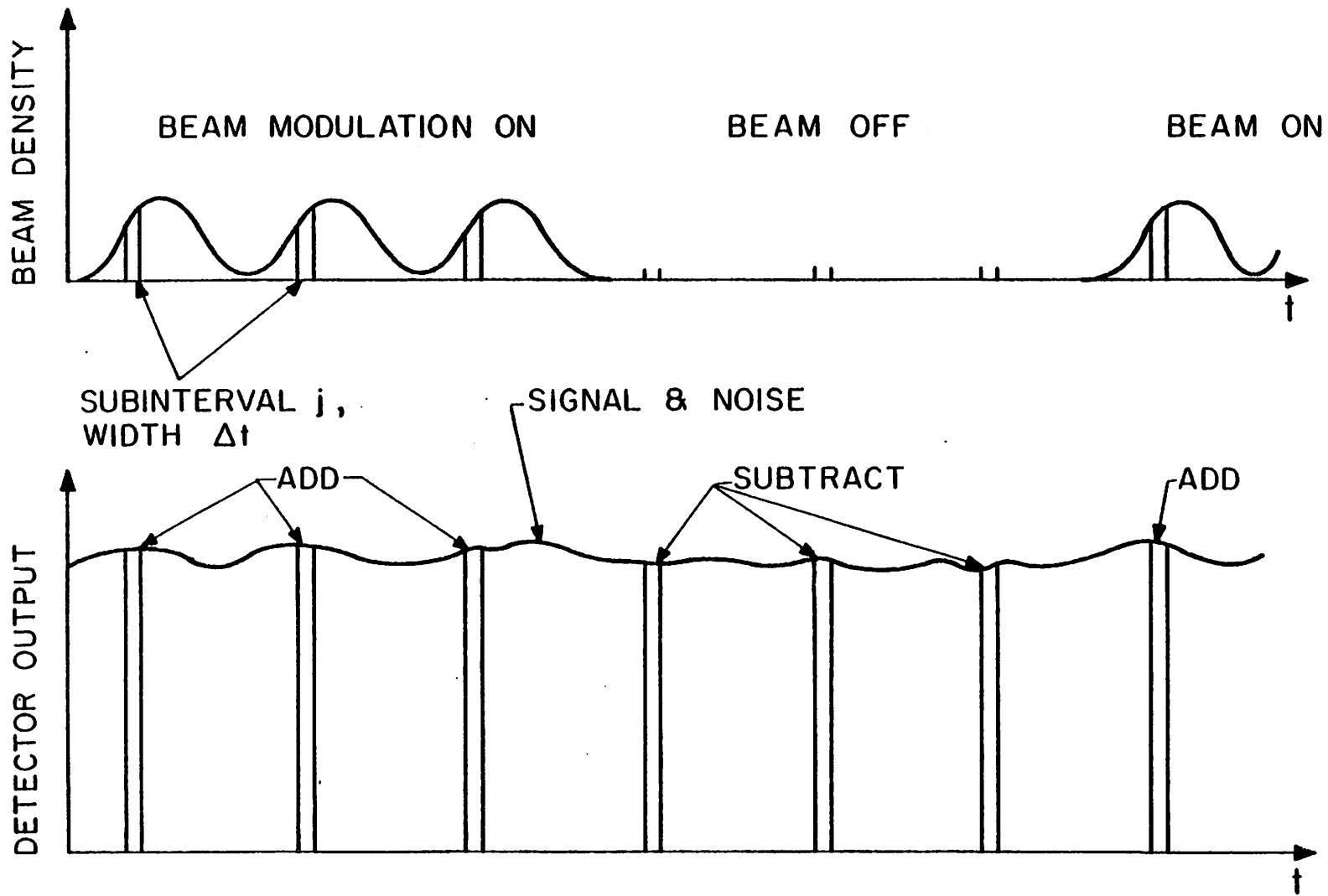


Fig. 10

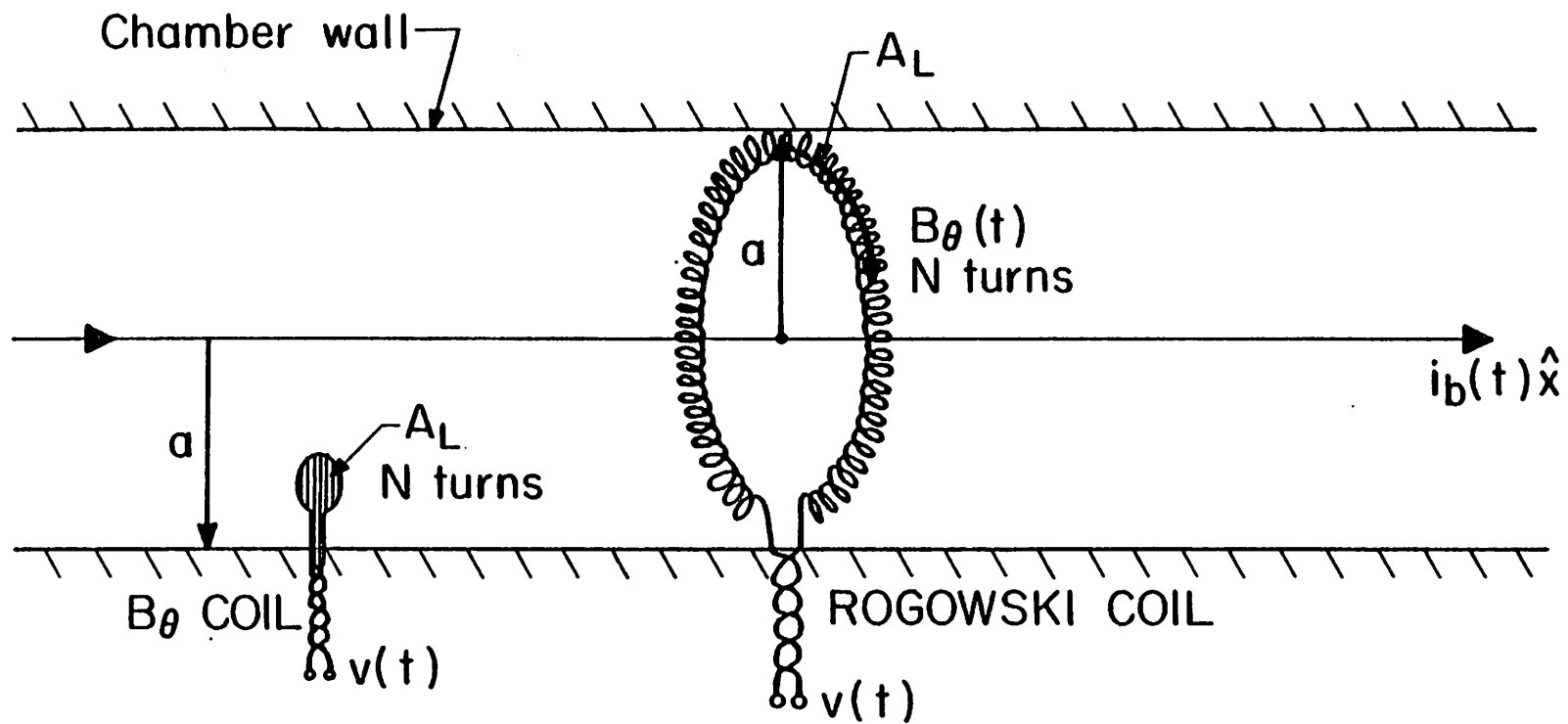
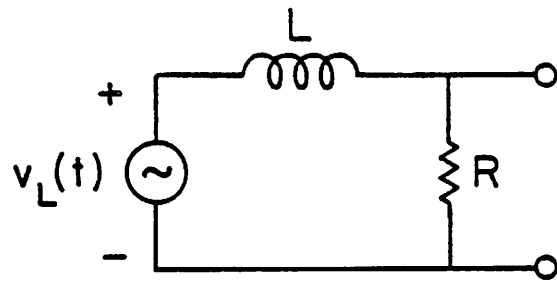
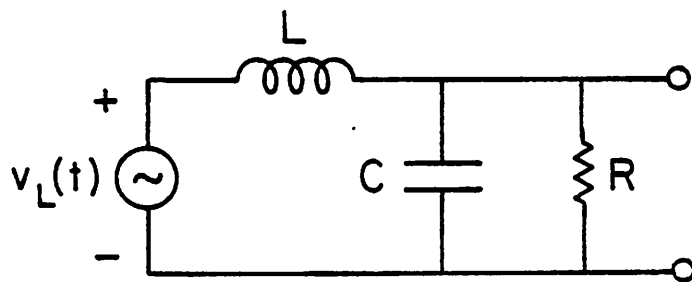


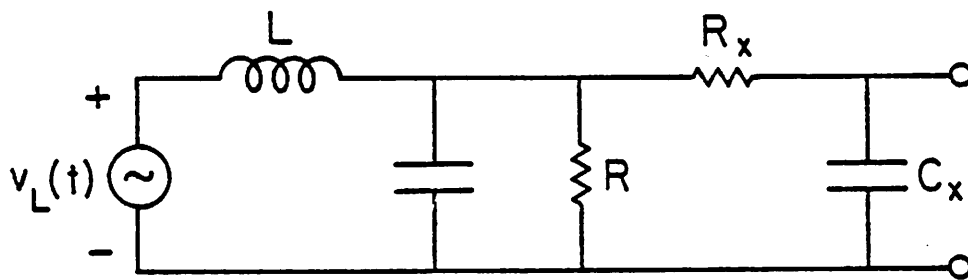
Fig. 11



(a)



(b)



(c)

Fig. 12

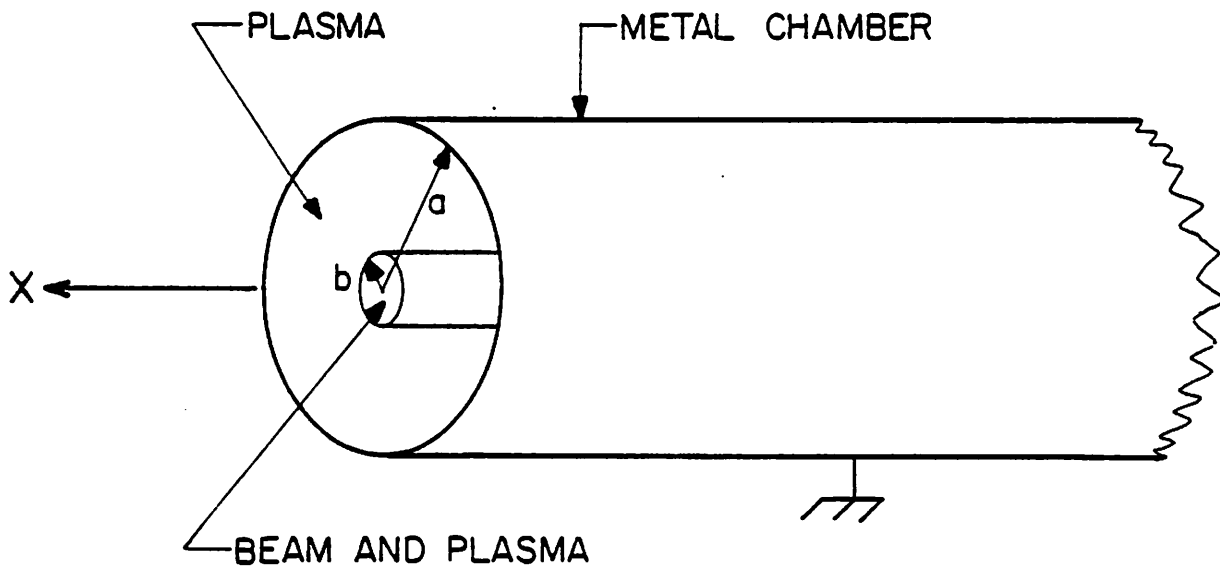


Fig. 13